Calibration Tools for Scanning Thermal Microscopy Probes Used in Temperature Measurement Mode

Tran Phong Nguyen, Laurent Thiery, Sébastien Euphrasie, Etienne Lemaire, S Khan, Danick Briand, Aigouy L, Séverine Gomes, Pascal Vairac

Calibration tools for Scanning Thermal Microscopy probes used in temperature measurement mode

TP Nguyen[1], L Thiery[1], S Euphrasie[1], E Lemaire[2], S Khan[2], D Briand[2], L Aigouy[3], S Gomes[4] and P Vairac[1]

[1] FEMTO-ST Institute, UMR 6174, Université de Franche-Comté, CNRS, ENSMM, UTBM, France
[2] Ecole Polytechnique Fédérale de Lausanne, Soft Transducers Laboratory, Neuchâtel, Switzerland
[3] LPEM, ESPCI Paris, CNRS, PSL Research University, Sorbonne Universités, Paris, France
[4] CETHIL, UMR5008, Univ Lyon, CNRS, INSA-Lyon, Université Claude Bernard Lyon 1, Villeurbanne, France
E-mail: laurent.thiery@univ-fcomte.fr

Abstract

We demonstrate the functionality of a new active thermal microchip dedicated to the temperature calibration of Scanning Thermal Microscopy (SThM) probes. The silicon micromachined device consists in a suspended thin dielectric membrane in which a heating resistor with a circular area of 50 µm in diameter was embedded. A circular calibration target of 10 µm in diameter was patterned at the centre and on top of the membrane on which the SThM probe can land. This target is a resistive temperature detector (RTD) that measures the surface temperature of the sample at the level of the contact area. This allows evaluating the ability of any SThM probe to measure a surface temperature in ambient air conditions. Furthermore, by looking at the thermal balance of the device, the heat dissipated through the probe and the different thermal resistances involved at the contact can be estimated. A comparison of the results obtained for two different SThM probes, micro-thermocouples and probes with a fluorescent particle is presented to validate the functionality of the micromachined device. Based on experiments and simulations, an analysis of the behaviour of probes allows pointing out their performances and limits depending on the sample characteristics whose role is always preponderant. Finally, we also show that a smaller area of the temperature sensor would be required to assess the local disturbance at the contact point.

Keywords: scanning thermal microscopy, temperature measurement, calibration, micro-hotplate

1. Introduction

Scanning Thermal Microscope (SThM) has become a major tool for investigating heat transfer at very low scales. Derived from Atomic Force Microscope (AFM), most of the systems can operate in two complementary modes, either in passive mode for surface temperature measurements [1], or in active mode for the estimation of parameters with a thermal or temperature dependence, i.e. the thermal conductivity or diffusivity [2]. The sensing elements are mainly based on the thermoresistive and the thermoelectric principles due to their ability to operate in both modes [3]. However, in temperature measurement mode, other kinds of sensors have been used, based on fluorescence or Raman spectroscopy for instance [4]. In any case, the measurements are performed by contacting a local probe on the surface to ensure the best possible lateral resolution. Unlike force interaction used for topographical images, tip-to-surface thermal interaction involves coupling effects that link both the probe and the sample characteristics. As a result, temperature measurements remain questionable in terms of accuracy due to the inevitable disturbance that the probe induces on the sample surface [5]. As simple as it sounds, this represents a fundamental question in thermal metrology. This question remains of major interest because despite the efforts made for years to improve SThM techniques, none of

the SThM users has ever presented the evidence of the accuracy of their probe to provide the actual temperature except some cases for which Raman spectroscopy was coupled to SThM [6-8]. Other presented measurements are always supported by simulations using the finite element method (FEM) as a validation method. Though the approach is questionable, the reported measurements only confirm that the probe is used in a favourable situation (i.e. on bulkier samples) [9-14]. Therefore, the only possible way to solve this problem is to eliminate heat transfer between the probe and the surface, by means of the so-called "null point method" [15,16]. Another method that eliminates the tip–sample contact-related artifacts, a major hurdle that has limited so far the use of SThM for nanoscale thermometry, has been also recently proposed [17]. This method is however only applicable under vacuum and for a sample operating in a modulated regime. In any case, tools adapted for calibrating the ability of a probe to measure an absolute temperature in contact condition remain essential. Among different thermal calibration devices currently proposed, some are devoted to lateral spatial resolution or measuring the probe-to-surface heat flux [18-20]. Here, we present a calibration device that characterizes quantitavely a SThM probe operating in passive mode, notably:

- Its "thermal response", which corresponds to the temperature measurement error compared to the actual surface value;
- The dissipated heat and the thermal resistances involved in the contact.

The device consists of a thin film micro-hotplate structure on which a surface temperature sensor is integrated. This sensor is dedicated to the measurement of the sample surface temperature at the level of a target where the probe tip is landed on. A comparison between the temperature of the probe and the one from the target before and during contact provides direct information about the probe accuracy and the thermal disturbance that occurs during the contact. Moreover, a thermal balance analysis of the device before and during contact results in the extraction of the thermal resistances that characterize both the probe and the sample.
Only steady-state was considered since all measurements were performed in static mode. Each measurement point was obtained after a contact duration of one second, whereas several tens of milliseconds were necessary for the probe tip - calibration chip couple to reach its thermal equilibrium.
Four different SThM probes were tested in ambient air conditions to illustrate the calibration principle: two micro-thermocouple probes [1,2] and two STM probes equipped with a fluorescent particle on [21]. The analysis of the measurements and simulations reveals the differences in their main behaviour and leads to propositions for improving both the probes and the calibration device.

2. Design and fabrication

For years, micro-hotplates are thermal components commonly used in microsystems such as semiconductor gas sensors, micro-calorimeters, and high sensitive flow meters [22-25]. The key element of such microsystem is a thermally isolated area, which is generally a silicon nitride thin membrane that can be heated by means of an embedded resistor. The temperature of this resistor can be precisely adjusted and controlled up to several hundred degrees above ambient. This principle has already been extended to develop a temperature calibration micro-chip for SThM probes [11]. Based on these previous results and supported by finite element method simulations (see section 3), the design has been optimized to reach the best compromise between robustness and reliability. The power consumption has also been reduced to increase the device sensitivity and the temperature distribution minimized using a circular symmetry for the design. As a result, only a power of 1.5 mW is required to heat up the central part at 100°C typically whereas 5 mW was required in the previous version of calibration devices [20]. To reach this performance and as represented in Fig. 1, the heater has been reduced to a 50 µm wide circular area instead of 220 × 220 µm² square area.

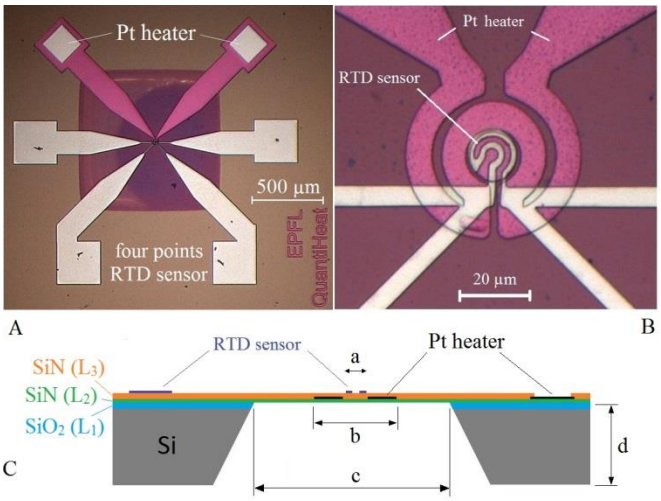

Fig. 1. Calibration chips with heating area of 50 µm in diameter and RTD contact area of 10 µm in diameter: Optical images of device top view (A), central area top view (B), and schematic of the device cross section (C).

The heating resistor is sandwiched in a suspended silicon nitride membrane of 1 mm² to ensure thermal insulation from the silicon frame of the chip. Furthermore, instead of being located aside the heater, the four wire surface RTD sensor has been patterned centrally on the heater area to increase the thermal sensitivity and ensure its temperature homogeneity. Covering a circular surface of 10 µm in diameter, it represents the target on which the SThM probe has to land. Table 1 summarizes the micro-chip main characteristics.

Table 1 Chip characteristics

	materials	thickness	dimension
RTD sensor	Ta+Pt	10+140 nm	a=10 µm
membrane	SiN (layer L_2) SiN (layer L_3)	L_2=200 nm L_3=400 nm	c=1 mm square c×c
heater	Ta+Pt	15+135 nm	b=50 µm
substrate	Si+SiO_2 (L_1)	d=390 µm L_1=500 nm	/

The fabrication process follows these steps:
First, a 500 nm-thick silicon oxide (L_1 in Fig. 2) is thermally grown on both sides of the wafer (390 µm-thick double side polished silicon wafer) to be used as etch-stop during the silicon back etching process. During the second step, a 200 nm low-stress Low Pressure Chemical Vapor Deposition (LPCVD) SiN is deposited (L_2). Then, a 15 nm Ta/135 nm Pt thin film is deposited using e-beam-evaporation and patterned via a lift off process in order to define the resistive heating elements. Another 400 nm thick low-stress LPCVD SiN (L_3) is deposited on top and contact windows on the heater contact pads are opened using reactive ion etching. This step is followed by the deposition of a 10 nm Ta/140 nm Pt thin film by e-beam-evaporation, which is patterned via a lift-off process using precise UV photolithography in order to define the resistive temperature sensors (RTD). Finally, the release of the SiN membrane consists in the bulk etching of the silicon wafer by Deep Reactive Ion Etching (DRIE) process. The remaining SiO_2 layer used as etch stop is etched away in BHF solution. A final annealing step is performed at 400°C for 30 min in nitrogen to reduce residual stress and stabilize the platinum films.
The resistance value of the heater and RTD is of 90 and 60 ohms, respectively. The chips have been calibrated to measure the temperature coefficient of the electrical resistance (TCR) of the RTD sensor. Measurements were performed in a programmable oven equipped with a Pt1000 reference temperature located next to the tested chip. The RTD sensor exhibited a mean TCR value of 0.00179 ±0.5% K^{-1} in the range 20°C to 120°C.

3. Simulation

To support the thermal design of the calibration chip, FEM simulations were performed using Comsol Multiphysics® software. Comparison between two-dimensional (2D) and three-dimensional (3D) simulations showed hardly no difference in a previous thermal calibration device [20]. A 2D model was therefore used here since it requires less computing time. A coupled electro-thermal model was used to simulate the heat source by Joule effect and its dissipation. Consequently, for each domain, the equation to be solved is:

$$-\nabla (k \nabla T) = Q + h (T_a - T) \qquad (1)$$

where Q is the power density due to Joule effect and h is the surface heat loss coefficient depending on the local temperature T. T_a is the ambient temperature and k is the effective thermal conductivity whose value is a weighted average depending on the sample local composition (thickness and material nature). The geometry implemented in the simulation comes from the mask design. The edges of the SiN membrane are surrounded by a silicon frame corresponding to the total size of the chip: 3 mm × 3 mm × 390 µm. Since the electrical conductivity of thin films are usually lower than bulk conductivity, the electrical conductivities of the heater and RTD layers were adjusted to fit the experimental values of the electrical resistances. According to Wiedemann-Franz law the ratio between the electrical conductivity of thin films and bulk materials was also applied to estimate the thermal conductivity of thin films. The TCR of the RTD sensor has been adjusted according to the calibration value extracted from the fabricated devices. The TCR of the heater was chosen so that both its electrical resistance and the temperature reached match the experimental values at a given power. The resulting TCR is coherent with measured one as shown in Table 2.
To describe the surface heat loss, a model assuming a linear variation of h with T has been chosen (h = AT +B). The two parameters (A and B) of the linear variation along with the value of the thermal conductivity of the SiN membrane have been set according to an iterative process. This iterative process compares experimental and simulation values of the temperature gradient observed between the edge of the active heating area and the interface membrane-silicon frame at different heater powers. The external surface heat loss coefficient h was found to be 50 W m^{-2} K^{-1} at ambient temperature with a linear increase of 1 W m^{-2} K^{-1} per Kelvin. The value of the thermal conductivity of the SiN membrane (k_{SiN}) was found to be 8 W m^{-1} K^{-1}. This value is in good agreement with the values published elsewhere. The reported values for k_{SiN} mainly ranged from 30 to 15 W m^{-1} K^{-1} [26] down to 3 W m^{-1} K^{-1} for low stress SiN films [27]. Indeed, the thermal conductivity of LPCVD SiN thin films depends on its resulting composition and density. Table 2 gives the thermo-electrical parameters used in our simulations.

Table 2 Materials electro-thermal simulation parameters

Material	k ($Wm^{-1}K^{-1}$)	ρ_e (Ω.m)	TCR (K^{-1})
RTD Ta/Pt film	39.6	$2.04\ 10^{-7}$	0.00179
Heater Ta/Pt film	28.8	$2.81\ 10^{-7}$	0.0018
SiN membrane	8	/	/
Si substrate	148	/	/

Figure 2 presents FEM simulation results in terms of temperature field at the device surface when the heater is supplied with a current of 4 mA, which corresponds to a power of 1.6 mW. As already discussed, we can verify in Fig. 2 that the new design of the resistive heating elements (dimension and shape) results in a central thermally homogeneous area. A comparison with the temperature measurements performed with a micro-thermocouple probe while the device dissipates the same power (1.6 mW) is given in section 6 (see Fig. 8). The good agreement obtained between the measurements and simulations demonstrates the

relevance of the modelling developed for designing the calibration chip.

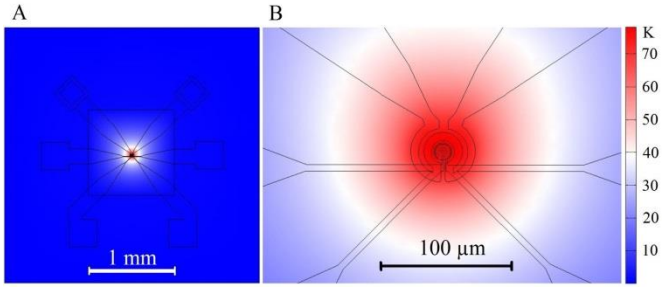

Fig. 2. FEM simulation temperature map obtained for an input power of 1.6 mW. Top view of the complete device (A) and zoom of the central area (B).

4. Challenges in measuring temperature using SThM probes

Regardless of the size of the thermal probe, the fundamental aspect of temperature measurement using a contact probe has been thoroughly analysed in several works [28-32]. The first question when trying to perform a contact temperature measurement relies on the disturbance that such measurement can arise. Two situations may occur according to the available heat power from the hot element to be tested and the heat absorbed by the probe contact itself. On one hand, the probe is thermally transparent and the measurement error is due to the state of the probe/surface contact. On the other hand, the heat absorbed by the probe is sufficient to cool down the sample which cannot supply the heat power required to keep its own temperature unchanged. In this last case, the origin of the measurement error mainly stems from the sample itself through its own thermal resistance that is usually called macro-constriction resistance or spreading resistance [5,28]. Figure 3 depicts the general aspect of a contact temperature measurement.

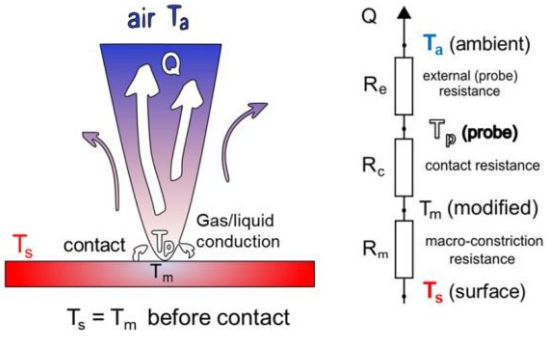

Fig. 3. Thermal configuration of a local temperature probe in contact with a hot surface.

According to this figure, the heat dissipated from the hot surface to the probe, Q, can be written as:

$$Q = \frac{T_s - T_m}{R_m} = \frac{T_m - T_p}{R_c} = \frac{T_p - T_a}{R_e} = \frac{T_s - T_a}{R_m + R_c + R_e} \qquad (2)$$

where T_s represents the actual surface temperature without probe, T_m is the surface temperature underneath the probe during contact, T_a is the ambient temperature and T_p is the value given by the probe.

The first parameter to be identified in the frame of the characterization of a temperature probe corresponds to the thermal response of the probe given by the ratio:

$$\tau = \frac{T_p - T_a}{T_s - T_a} = \frac{R_e}{R_m + R_c + R_e} \qquad (3)$$

This can be identified as a measurement error since a perfect probe or a null-point method should lead to τ=1. In addition to the direct measurement of the thermal response, the estimation of the different thermal resistances involved in the contact requires the extraction of the heat absorbed by the probe Q, which remains difficult. Indeed, realistic cases of contacting a probe onto a sample take place between two limiting cases:

- Case 1 of a transparent probe when R_e tends to infinity or Q is negligible. This also corresponds to a negligible macro-constriction resistance R_m when the sample cannot be perturbed; either this sample is massive in size or a large amount of heat compensates the dissipation heat Q. In this case the surface temperature before contact T_s remains unchanged and T_m equals T_s;

- Case 2 of a huge effect of the probe during contact when R_e is low. This also corresponds to an important macro-constriction resistance R_m of a very tiny sample and/or a very low available heat power regarding the dissipated heat Q. Here T_m is very different from T_s.

As a result, T_m values logically range between T_a and T_s and a subsequent question remains on the spatial distribution of T_m; is it a "cold spot" underneath the tip contact or does the perturbation spreads enough to modify the whole surface ? Clearly, previous works have shown that such a thin membrane structure is subjected to a global temperature change [20]. This justifies the use of a 10 µm diameter surface RTD sensor that allows a direct measurement of the modified surface temperature T_m without the necessity to locate the tip contact at the very central point of the RTD target. This effect will be confirmed later in this paper by FEM simulations and measurements (see Fig. 8 to 10). We then assume in the following reasoning that the RTD sensor is large enough to provide a relevant temperature value of the central membrane area without being perturbed by the possible cold contact point. It will be shown below that the cold point underneath the tip contact is too small to affect the RTD value. Therefore, one can define a linear relationship between the central surface temperature given by the RTD sensor and the dissipated power both with and without a probe contact (see Fig. 6).

First, without any contact, the electrical power applied to the device P_0 dissipates to ambient, by convection with ambient

air, radiation to the device surrounding (radiative heat loss can be assumed linear with temperature at temperatures around T_a) and conduction to the chip silicon substrate. This can be written using a global heat transfer expression:

$$P_0 = K_0(T_s - T_a) \qquad (4)$$

where K_0 represents the global thermal conductance between the calibration device and the ambient environment (without contacting probe), T_s being provided by the RTD sensor.
Second, when a probe contacts the sample, the surface temperature changes as indicated by the RTD sensor with T_m. However, the new power supplied electrically is dissipated to ambient through the contact probe in addition to the same global conductance K_0, then:

$$P_1 = K_0(T_m - T_a) + Q \qquad (5)$$

Here, we assume that the probe contact does not change the dissipation mode of the device. This is due to the probes geometry (thin wires and tungsten tip, as shown in figures 4 and 5), positioned perpendicularly to the surface over a large distance, which can be considered as not affecting significantly the boundary layer above the surface of the membrane.
Expression (2) provides a relationship between the probe temperature and its thermal resistance:

$$Q = \frac{T_p - T_a}{R_e} \qquad (6)$$

The new thermal balance of the coupled probe-surface allows the identification of a new global conductance K_1 including the probe effect so that:

$$P_1 = K_1(T_m - T_a) \qquad (7)$$

All the temperatures can be measured and plotted versus the input power so that K_0 and K_1 are directly identified. This provides a direct access to the thermal resistance of the probe by combining expressions (5), (6) and (7):

$$R_e = \frac{T_p - T_a}{(K_1 - K_0)(T_m - T_a)} \qquad (8)$$

It follows that the other thermal resistances of the probe-sample system can be deduced from expression (2):

$$R_c = R_e \frac{T_m - T_p}{T_p - T_a} = R_e \left(\frac{T_m - T_a}{T_p - T_a} - 1 \right) \qquad (9)$$

and

$$R_m = (R_c + R_e) \frac{T_s - T_m}{T_m - T_a} = (R_c + R_e) \left(\frac{T_s - T_a}{T_m - T_a} - 1 \right) \qquad (10)$$

Among all of these parameters that characterize the coupled behaviour between a probe and the calibration device:

- only R_e represents an intrinsic parameter of the probe;
- the contact resistance R_c gives an indication of the contact state but can vary with the thermomechanical properties and the roughness of surfaces;
- the other quantities such as τ or R_m are only relevant in the frame of a round robin test between different temperature probes since they are closely related to the calibration chip characteristics.

In the following, the thermal response τ and the different thermal resistances R_e, R_c and R_m will be extracted in the temperature range from ambient to about 100°C, using the four different probes.

5. Tested SThM probes

Four different SThM probes have been tested to evaluate the calibration device functionality: two micro-thermocouples on quartz tuning fork (QTF) and two fluorescent particle-based tips. Micro-thermocouples have been extensively used in various applications, and adapted to scanning thermal microscopy in both operating modes for temperature (passive mode) and thermal conductivity (active mode) measurements [1,2,5]. They are made with Wollaston wires of platinum and platinum-rhodium (90%/10%) alloy to obtain a S type thermoelectric couple. Fig. 4(A) presents the general aspect of a probe developed for SThM applications.

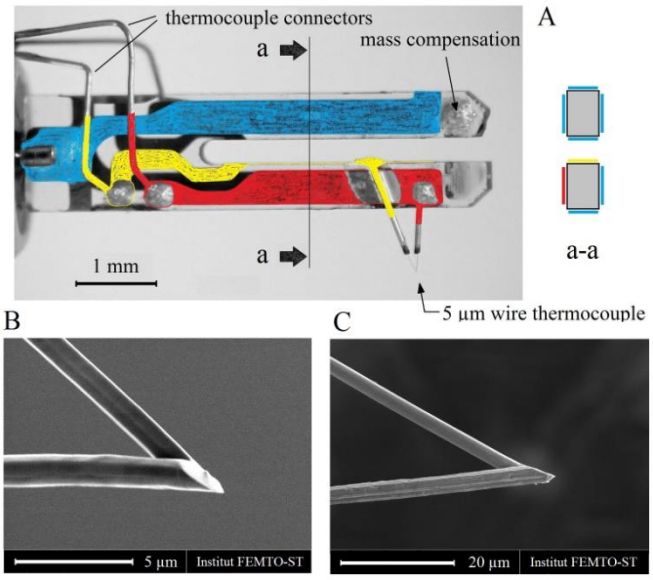

Fig. 4. Micro-wire thermocouple probe on quartz tuning fork. A: Structure and connecting overview; B: 1.3 µm wire junction and C: 5 µm wire junction scanning electron microscopy (SEM) images.

Here the use of a quartz tuning fork allows controlling the force when a contact between the tip and a sample occurs [33]. The thermocouple is embedded on a QTF prong and electrically connected to two electrodes previously disconnected from the QTF. The embedded mass is then sufficiently low to preserve a quality factor near 8000 in air. A modulated photothermal excitation is used at the resonance frequency of the QTF (near 32 kHz) whose shifting

frequency value is controlled to detect a contact between the thermocouple tip and a sample with a fixed force in the range of some tens of nanonewtons. Figure 4(B) and (C) present the thermocouple junctions fabricated from wires with diameter of 1.3 µm and 5 µm respectively. The junction of each fabricated probe is systematically reshaped by means of a focused ion beam (FIB) in order to refine the tip apex and optimize the probe spatial resolution.

In parallel to thermocouple probes, fluorescence thermometry represents an available alternative to measure the temperature of micro-devices with a submicron spatial resolution [11,21]. In that case, we used a fluoride KY_3F_{10}/YF_3 nanocrystal doped with Er^{3+} ions [21]. Such materials possess two fluorescence lines (located at 525 nm and 545 nm) that come from energy levels that are in thermal equilibrium. The relative importance of their intensities (the intensity ratio) is directly linked to temperature. The nanocrystal (size = 200-300 nm) is glued at the end of a sharp tungsten tip and excited with a low power 658 nm laser diode (250 µW). The fluorescence is recorded with a spectrometer. We show in Fig. 5 a SEM picture of an example of tip with the nanocrystal attached at its end. In these works the tip, actuated with a piezo-electric disk, was placed in contact with the sample and oscillated (frequency = 5 kHz) on the surface. To improve the heat transfers between the surface and the tip, the measurements were performed with an oscillation amplitude strongly damped compared to the free space one (damping offset = 80%). Two fluorescent tips were used in this study, with a shape similar to the one shown in Fig. 5. They differ by the shape, the orientation and the position of the nanocrystal at the end of the tip, and by the angle of the tungsten cone which slightly varies from a tip to another.

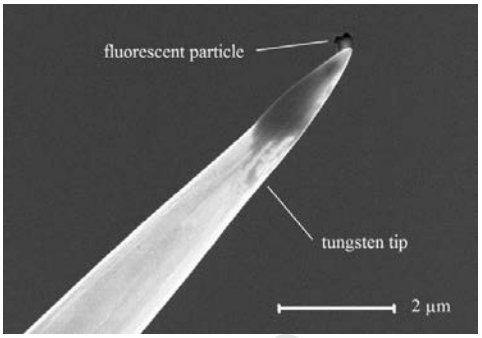

Fig. 5. SEM picture of an example of tungsten tip with a fluorescent nanocrystal glued at its end.

6. Results and discussion

Figure 6 reports the measurements performed with the tested probes. They were performed in the temperature range 20 to 100°C which corresponds to the usual operating range of most SThM probes. These measurements were obtained on the same calibration device and under similar ambient air conditions (T_a around 22°C and relative humidity near 50%). The RTD surface temperature was calculated considering a TCR of 0.00179 K^{-1} and a reference for the electrical resistance of the RTD measured at T_a. For each value of power, thermocouple probes were put in contact five times successively with the same contact force (about 20 nanonewtons) in order to reduce uncertainties. Two successive sets of measurements were performed with the fluorescent probe. The analysis of these results per probe used has been made considering the mean value of these measurements. Error bars indicate a standard uncertainty of ±1 K for the temperatures measured by means of thermocouples, a relative uncertainty of ±1% for the temperature values from the RTD sensor, and ±10% for the temperature measured by the fluorescent probe.

Figure 6 depicts the different temperature elevation from ambient versus the input power of the calibration device. (T_s-T_a) represents the RTD sensor response without probe contact whereas (T_m-T_a) is measured during contact of the four different probes, each of them providing their own values (T_p-T_a). It is interesting to notice the linearity of the temperatures versus the input power of the calibration device. As a result, thermal conductances and resistances can be assumed as constant values. The extracted slopes obtained by means of a least square method allow to calculate at the same time thermal conductance at ambient K_0 (no contact) and K_1 for each of the probes, and the values of thermal resistances R_e, R_c and R_m. These values are summarized in Table 3, in addition to the probes thermal responses τ.

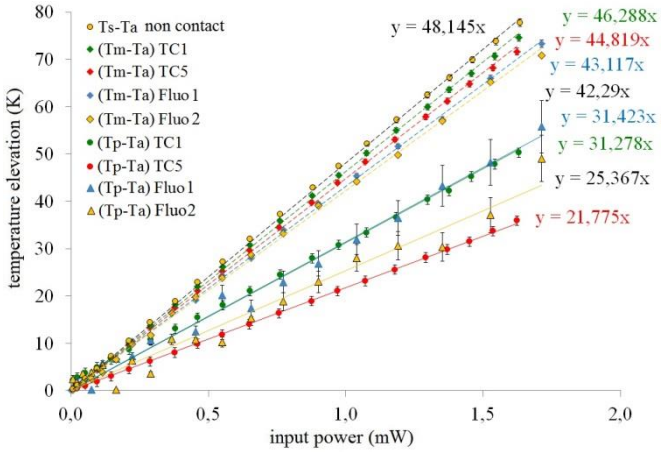

Fig. 6. Temperature elevations from T_a as a function of the input power: for each of the four probes tested (T_s-T_a) and (T_m-T_a) measured by the RTD sensor without and with probe contact respectively, and (T_p-T_a) given by the probe. TC1 and TC5 represent the thermocouple probes of 1.3 µm and 5 µm wire diameters respectively, Fluo1 and Fluo 2 the two tungsten tip probes equipped with a fluorescent particle.

Table 3 Measurement results (K_0 =20.77 10^{-6} W K^{-1})

	K_1 (W K^{-1})	τ	Re (K W^{-1})	Rc (K W^{-1})	Rm (K W^{-1})
TC1	21.60 10^{-6}	0.65	8.11 10^5	3.89 10^5	48161

TC5	22.31 10^{-6}	0.45	3.15 10^{5}	3.34 10^{5}	48157
Fluo1	23.19 10^{-6}	0.67	3.95 10^{5}	1.47 10^{5}	46851
Fluo2	23.64 10^{-6}	0.54	2.43 10^{5}	1.62 10^{5}	47312

As expected, Table 3 shows that TC5 exhibits the worst results due to its large size. Inversely, Fluo1 probe provides the highest thermal response, slightly higher than the one to the smallest thermocouple TC1. One could expect a larger difference between these two probes since the dimension of the STM tungsten Fluo tip appears to be the thinnest among all others. However, a simple calculation can easily demonstrate that the two main characteristics that govern the internal thermal resistance of a conical taper are the thermal conductivity and the tip cone angle. Tungsten thermal conductivity value is 173 $Wm^{-1}K^{-1}$ at ambient. It acts as a limiting factor that explains the relatively low resistance R_e of the probe. Inversely, this thermal conductivity may be responsible of a lower thermal contact resistance, R_c, in comparison to TC probes since it helps to heat up the fluorescent particle. As a result, fluorescent probes exhibit lower contact thermal resistances than thermocouple probes. Logically, the values of the macro-constriction resistance that characterizes the calibration chip are almost identical.

6.1 Role of the sample nature

An interesting comparison can be made between TC1 and Fluo1 probes since their thermal response are similar although their thermal resistances are quite different. Whereas TC1 could be improved by decreasing its contact resistance R_c, Fluo1 would require to increase its internal resistance R_e, by reducing its thermal conductivity typically. Furthermore, since the heat dissipated by the probe contact results from the sum of the different resistances (R_e+R_c+R_m), it appears that the heat dissipated by Fluo1 probe is more than twice superior to the TC1 probe. This represents a major problem when trying to measure the temperature of a thinner object such as a nanowire. In the present situation however, the lower contact resistance helps to reduce the temperature difference between T_p and T_m, then with T_s. Figure 7 illustrates these differences of behaviour by simply comparing their respective thermal response versus sample macro-constriction resistance R_m, with fixed R_e and R_c from Table 3.

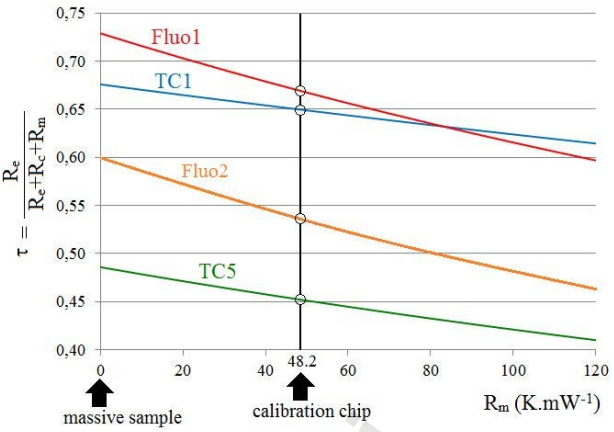

Fig. 7. Influence of the sample nature (R_m) on the resulting thermal response (τ) of the different probes, R_e and R_c being extracted from Table 3.

The data related to the calibration chip used correspond to the abscissa 48.2 K mW^{-1} and a simulated massive sample is located at the origin. This clearly demonstrates the influence of the sample characteristics on the probe behaviour.

6.2 Experimental validation of FEM simulations

Following these results, the TC1 probe was used to perform a scan of the central area (200 × 200 µm² and 100 × 100 pixels) of the calibration device. The device was then supplied with a power of 1.6 mW for comparison with the simulations presented in Fig. 2. The correction factor τ of 0.65 was applied to the measured temperature so that the indicated temperature scales of Fig. 8(A) represents the actual value of (T_s-T_a) (no contact). As shown in simulation results (Fig. 2), the temperature distribution is symmetrical around the central point where the RTD sensor is located.

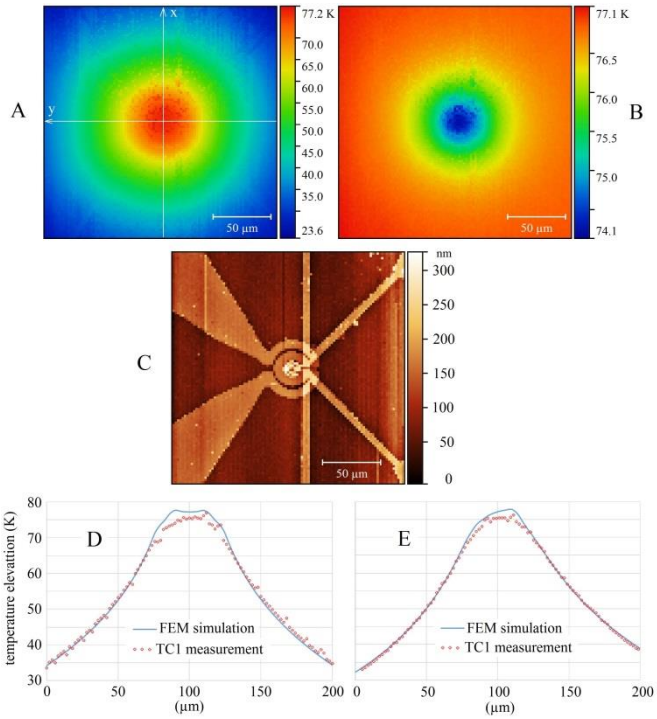

Fig. 8. TC1 probe 200 × 200 µm² scan results at 1.6 mW of input power. A: Corrected temperature map; B: RTD sensor response; C: topography; D and E: extracted temperatures along the x and y axis of image A superimposed with FEM simulated profiles.

Figure 8(B) shows the temperature response provided by the RTD sensor during the scan of the device surface by TC1. It confirms that the thermal disturbance is both symmetrical around the centre and spreading farther than the RTD sensor area. The RTD sensor exhibits a cooling down practically unchanged when the TC1 probe tip stays in the central area of about 20 µm of diameter. This is not only due to the spatial integration effect of the RTD sensor but also confirms the spreading distance of the thermal perturbation.

Figure 8(C) depicts the topographical image given from the QTF response of the probe. In Fig. 8(D) and Fig. 8(E), the values extracted along the x and y axis from the Fig. 8(A) (white axes) have been superimposed to the simulated profile. The good correlation between FEM simulation and measurements is demonstrated. The slight dissymmetry along y axis, also visible in Fig. 2, is confirmed experimentally. This is due to the platinum leads of the heater that increases heat conduction to the silicon substrate. These two images also point out an important advantage of a micro-thermocouple on QTF probe in comparison to the usual cantilever type SThM probes; there is no parasitic heat transfer between the hot sample surface and the QTF prong due to the distance between them. This distance exceeds 1 mm typically.

6.3 Cold contact point effect

Assuming our simulation results as close enough to reality, we have explored the effects of the probe contact for the four probes used in this work. When a contact occurs, the heat dissipation through the probe corresponds to the ratio:

$$Q = \frac{T_m - T_a}{R_c + R_e} \qquad (11)$$

T_m is assumed to correspond to the surface RTD sensor value, R_c and R_e are given by Table 3 for the four probes used. The resulting heat flux can be applied to the central contact area. However, the main question remains on the thermal contact radius of the probe. Under vacuum, this radius is given by the solid-solid contact radius that depends on the mechanical properties of both the surface and probe tip, leading to values in the range of some nanometers. In ambient environment, heat transfer through air is preponderant so that this radius is much larger. This is a complex problem that cannot be treated in the present article, so that we have chosen two likely values stemmed from our own experience: 1 µm and 200 nm. Figure 9 depicts the x axis temperature distribution at the same supplied power than results of Fig. 8, while there is no contact and when using the four probes and a thermal contact radius of 1 µm.

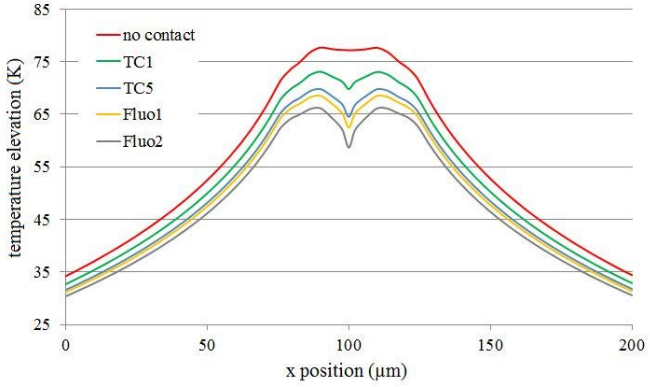

Fig. 9. FEM simulation temperature distribution along x axis before contact (red line) and considering extracted values of (R_c+R_e) of Table 3 representing the four probes contact effects with a 1 µm thermal contact radius.

The effect of a global cooling of the membrane in addition to a localized cold contact point is clearly visible. A closer view is given in Fig. 10 in which the effects of the thermal contact radius have been superimposed. Continuous lines correspond with a 1 µm radius and dashed lines to a 200 nm radius. The grey area represents the location of the RTD surface sensor of width 10 µm, whose temperature value corresponds to the dots at position 100 µm. It is interesting to notice that these integrated values – extracted from simulations – remain identical when varying the thermal contact radius between 200 nm and 1 µm, the difference staying below 0.5%. It appears clearly that more the radius decreases, more the cooling effect is spatially reduced.

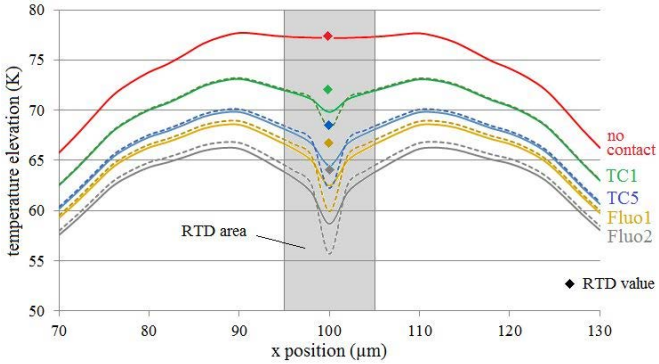

Fig. 10. FEM simulation x axis temperature distributions: comparison between 1 µm (solid lines) and 200 nm (dashed lines) thermal contact radius.

This result also significates that the cooling effect is not strictly homogeneous on the membrane. The consequences are however limited since the shape and size of the RTD sensor (see Fig. 1(B)) make it almost insensitive to the "cold spot" then providing relevant temperatures for a correct estimation of the dissipated heat Q, and subsequently the probe thermal resistance R_e.

Inversely, there is no correct evaluation of a reliable T_m value so that the extraction of R_c using expression (9) may lead to underestimated values. This is confirmed by simulations based on (R_c+R_e) values (Table 3) that provide mean temperatures of the RTD sensor slightly inferior to experimental ones: 72.0 K, 68.4 K, 66.7 K and 64.2 K instead of 74.0 K, 71.7 K, 69.0 K and 67.7 K for TC1, TC5, Fluo1 and Fluo2 probes, respectively. The remaining value for the R_m resistance that characterizes the calibration surface itself may also be underestimated.

7. Conclusion and perspectives

We propose a new calibration active device whose first objective is to provide a thermal response (τ) of any temperature probe used in SThM as well as the methodology of its application. The functionality of the device has been demonstrated on two different types of SThM probes: micro-thermocouple probe and STM tip with fluorescent particle on. Clearly, it would be of great interest to test other kinds of SThM probes, especially active probes that operate in null-point mode that should provide a perfect thermal response close to unity.

A simple thermal balance approach provides the heat dissipated by the probe and the estimation of the different thermal resistances involved at the contact. An intrinsic parameter of passive probes that corresponds to the internal thermal resistance R_e is extracted. Acting as a fin, the highest possible value is required to reduce the heat dissipation at the contact point. Inversely, an efficient contact requires a low contact thermal resistance R_c. However, it remains difficult to both increase R_e and decrease R_c. As shown in the results, due to their thin geometry and/or their low thermal conductivities, high R_e probes exhibit generally high R_c values due to a poor heat transfer efficiency at the contact point area, and inversely. On the other hand, the heat dissipated by the probe being conditioned by the sum R_e + R_c, we show that two probes having the same thermal response can behave very differently in terms of sample perturbation. We point out the importance of the sample nature through its macro-constriction resistance R_m that also conditions the thermal response.

The low dispersion in the R_m values reported in Table 3, below 2%, in addition to the use of T_m as an indicator of the temperature at the surface of the membrane, validates the additive assumption made in equations 4 and 5 on the heat dissipation of the device and the probe.

A comparison with FEM simulations tends to demonstrate that the cold point underneath the contact point of a probe is always significant. The surface RTD sensor used in this calibration device is however too large to highlight its existence but validate the assumptions made for the thermal balance analysis. As a consequence, the modified surface temperature called T_m accuracy is limited since it cannot allow the extraction of the contact thermal resistance R_c of the probes which are probably underestimated in this work. Instead of a RTD sensor, a more local temperature sensor such as a thin-film thermocouple may be a relevant mean to improve these results.

Acknowledgements

This work has received funding from the European Union Seventh Framework Program FP7-NMP-2013-LARGE-7 under GA No. 604668 Project QUANTIHEAT.

References

[1] Bontempi, A., Thiery, L., Teyssieux, D., Briand, D., Vairac, P., 2013, "Quantitative thermal microscopy using thermoelectric probe in passive mode", Rev. Sci. Instrum. 84, 103703.

[2] Bontempi, A., Nguyen, T.P., Salut, R., Thiery, L., Teyssieux, D., Vairac, P., 2016, "Scanning thermal microscopy based on a quartz tuning fork and a microthermocouple in active mode (2ω method)", Rev. Sci. Instrum. 87, 063702.

[3] Gomes, S., Lefevre, S., 2008, in Advanced Techniques and Applications on Scanning Probe Microscopy, edited by F. H. Lei (Research Signpost), 157–195.

[4] Gomes, S., Assy, A. and Chapuis, P.O., 2015, "Scanning Thermal Microscopy: a review", Phys. Status Solid A 212, 3, 477-494.

[5] Thiery, L., Toullier, S., Teyssieux, D., Briand, D., 2008, "Thermal contact calibration between a thermocouple probe and a microhotplate", J. Heat Transfer 130, 091601.

[6] Jo, I., Hsu, I.K., Lee, Y.J., Sadeghi, M.M., Kim, S., Cronin, S., Tutuc, E., Banerjee, S.K., Yao, Z. and Shi, L., 2011, "Low-frequency acoustic phonon temperature

distribution in electrically biased grapheme", Nanoletters 11, 85-90.

[7] Soudi, A., Dawson, R.D. and Gu, Y., 2011, "Quantitative heat dissipation characteristics in current-carrying GaN nanowires probed by combining scanning thermal microscopy and spatially resolved Raman spectroscopy", ACS Nano 5 (1), 255-262.

[8] Yu, Y.J., Han, M.Y., Berciaud, S., Georgescu, A.B., Heinz, T.F., Brus, L.E., Kim, K.S. and Kim, P., 2011, "High-resolution spatial mapping of the temperature distribution of a Joule self-heated grapheme nanoribbon", Appl. Phys. Lett. 99, 183105.

[9] Janus, P., Szmigiel, D., Weisheit, M., Wielgoszewski, G., Ritz, Y., Grabiec, P., Hecker, M., Gotszalk, T., Sulecki, P., Zschech, E., 2010, "Novel SThM nanoprobe for thermal properties investigation of micro- and nanoelectronic devices", Microelec. Engin, 87, 1370-1374.

[10] Wielgoszewski, G., Sulecki, P., Janus, P., Grabiec, P., Zschech, E. and Gotszalk, T., "A high resolution measurement system for novel scanning thermal microscopy resistive nanoprobe", 2011, Meas. Sci. & Tech. 22, 094023.

[11] Saïdi, E., Samson, B., Aigouy, L., Volz, S., Löw, P., Bergaud, C. and Mortier, M., 2009, "Scanning thermal imaging by near-field fluorescence spectroscopy", Nanotechnology 20, 115703.

[12] Sadat, S., Tan, A., Chua, Y.J. and Reddy, P., 2010, "Nanoscale thermometry using point contact thermocouples", Nanoletters 10, 2613-2617.

[13] Kim, K., Chung, J., Hwang, G., Kwon, O. and Lee, J.S., 2011, "Quantitative measurements with scanning thermal microscope by preventing the distorsion due to the heat transfer through the air", ACS Nano 5 (11), 8700-8709.

[14] Kim, K., Jeong, W., Lee, W. and Reddy, P., 2012, "Ultra-high vacuum scanning thermal microscopy for nanometer resolution quantitative thermometry", ACS Nano 6 (5), 4248-4257.

[15] Chung, J., Kim, K., Hwang, G., Kwon, O., Jung, S., Lee, J., Lee, J.W. and Kim, G.T., 2010, "Quantitative temperature measurement of an electrically heated carbon nanotube using the null-point method", Rev. Sci. Instrum. 81, 114901.

[16] Hwang, G., Chung, J. and Kwon, O., 2014, "Enabling low-noise null-point scanning thermal microscopy by the optimization of scanning thermal microscope probe through a rigorous theory of quantitative measurement", Rev. Sci. Instrum. 85 (11), 114901.

[17] Menges, F., Mensch, P., Schmid, H., Riel, H., Stemmer, A. and Gostmann, B., 2016, "Temperature mapping of operating nanoscale devices by scanning probe thermometry", Nature Communications 7, 10874.

[18] Ge, Y., Zhang, Y., Booth, J.A., Weaver, J.M.R. and Dobson, P.S., 2016, "Quantification of probe–sample interactions of a scanning thermal microscope using a nanofabricated calibration sample having programmable size", Nanotechnology 27, 325503.

[19] Varpula, A., Timofeev, A.V., Shchepetov, A., Grigoras, K., Hassel, J., Ahopelto, J., Ylilammi, M. and Prunnila, M., 2017, "Thermoelectric thermal detectors based on ultra-thin heavily doped single-crystal silicon membranes", Appl. Phys. Lett. 110, 262101.

[20] Nguyen, T.P., Lemaire, E., Euphrasie, S., Thiery, L., Teyssieux, D., Briand, D. and Vairac, P., 2018, "Microfabricated high temperature sensing platform dedicated to scanning thermal microscopy (SThM)", Sensors and Actuators A 275, 109–118.

[21] Assy, A., Lin, H.J., Schoenauer-Sebag, M., Gredin, P., Mortier, M., Billot, L., Chen, Z. and Aigouy, L., 2016, "Nanoscale thermometry with fluorescent yttrium-based Er/Yb-doped fluoride nanocrystals", Sensors and Actuators A 250, 71-77.

[22] Sarro, P.M., Van Herwaarden, A.W. and Van der Vlist, W., 1994, "A silicon-silicon nitride membrane fabrication process for smart thermal sensors", Sensors & Actuators A 42, 666-671.

[23] Simon, I., Barsan, N., Bauer, M. and Weimar, U., 2001, "Micromachined metal oxide gas sensors: opportunities to improve sensor performance", Sensors and Actuators B 73, 1-26.

[24] Rossi, C., Briand, D., Dumonteuil, M., Camps, T., Pham, P.Q. and De Rooij, N.F., 2006, "Matrix of 10×10 addressed solid propellant microthrusters: Review of the technologies", Sensors and Actuators A 126(1), 241-252.

[25] Konz, W., Hildenbrand, J., Bauersfeld, M., Hartwig, S., Lambrecht, A., Lehmann, V. and Wöllenstein, J., 2005, "Micromachined IR-source with excellent blackbody like behaviour", Proc. SPIE Vol 5836, 540-548.

[26] Plummer, J.D., Deal, M.D., Griffin, P.B., 2001, silicon VLSI Technology: Fundamentals, Practice, and modeling, ed. Pearson, ISBN-13: 9780130850379.

[27] Sultan, R., Avery, A.D., Underwood, J.M., Mason, S.J., Bassett, D. and Zink, B.L., 2013, "Heat transport by long mean free path vibrations in amorphous silicon nitride near room temperature", Phys. Rev. B, 87-21, 214305.

[28] Bardon, J.P., Cassagne, B., 1981, Ed. Techniques de l'Ingénieur, Traité de Mesures Physiques, chapitre R2732 : Temperature de surface, mesures par contact.

[29] Majumdar, A,. 1999, "Scanning Thermal Microscopy", Annu. Rev. Mater. Sci. 29, 505-585.

[30] Shi, L., Majumdar, A., 2002, “Thermal transport mechanisms at nanoscale point contacts”, J. Heat Transfer 124, 329-332.
[31] Gomes, S., Trannoy, N., Grossel, P., 1999, “DC thermal microscopy: study of the thermal exchange between a probe and a sample”, Meas. Sci. Technol. 10, 805-811.
[32] Lefevre, S., Volz, S. and Chapuis, P.O., 2006, “Nanoscale heat transfer at contact between a hot tip and a substrate”, Int. J. Heat and Mass Tranf. 49, 251-258.
[33] Bontempi, A., Teyssieux, D., Friedt, J.M., Thiery, L., Hermelin, D. and Vairac, P., 2014, “Photo-thermal quartz tuning fork excitation for dynamic mode atomic force microscope”, Appl. Phys. Lett. 105, 154104.